Nanoindentation characterization of sintered porous Cu nanoparticles used in power electronics packaging – A molecular dynamic simulation study

Hu, Dong; Li, Zichuan; Fan, Jiajie; Zhang, Guoqi

DOI
10.1109/EPTC59621.2023.10457748

Publication date
2023

Document Version
Final published version

Published in
Proceedings of the 25th Electronics Packaging Technology Conference, EPTC 2023

Nanoindentation characterization of sintered porous Cu nanoparticles used in power electronics packaging – A molecular dynamic simulation study

Dong Hu[1], Zichuan Li[1], Jiajie Fan[1,2,3], Guoqi Zhang[1#]
1 EEMCS Faculty, Delft University of Technology, Delft 2628CD, the Netherlands
2 Institute of Future Lighting, Academy for Engineering & Technology; Shanghai Engineering Technology Research Center for SiC Power Device, Fudan University, Shanghai 200433, China
3 Research Institute of Fudan University in Ningbo, Ningbo 315336, China
#Corresponding: g.q.zhang@tudelft.nl

2023 IEEE 25th Electronics Packaging Technology Conference (EPTC) | 979-8-3503-2957-5/23/$31.00 ©2023 IEEE | DOI: 10.1109/EPTC59621.2023.10457748

Abstract

As a critical part of speeding up industrial electrification, power electronics, and its packaging technology are undergoing rapid development. Cu nanoparticle sintering technology has therefore received extensive attention for its excellent performance in the die-attachment layer, where the mechanical properties are essential to be known for design for reliability. Both sintering and subsequent nanoindentation were studied by simulation. The effect of porosity on the nanoindentation response was investigated by setting different initial packing densities. In addition, the impact of indenter size and indentation positions on the nanoindentation response were discussed. The nanoindentation behaviors were studied by extracting loading-displacement (*P-h*) curves and calculating elastic modulus and hardness. In addition, the microstructure evolution was adopted using atomic configuration to study the nanoindentation mechanism. This work offers valuable insights into the Cu sinter paste preparation phase for sintering technology.

Keywords: Nanoindentation, Sintering technology, Cu nanoparticles, molecular dynamics

Introduction

In the *'More than Moore'* concept, power electronics is a significant domain as it speeds up industrial electrification [1]. Driven by the rapid development of wide-bandgap semiconductor, represented by silicon carbide (SiC) and gallium nitride (GaN), enormous attention have been attached to power electronics packaging [2], [3]. Conventional die-attachment technologies face challenges in high-temperature reliability performance according to the continuously increasing demand for a higher power density and operating temperatures [4].

Over the last decade, Ag and Cu nanoparticle (NP) sintering technology has become a promising candidate in lead-free die-attachment with excellent thermal and electrical performances [5]–[8]. Therefore, it is urgent to understand the thermos-mechanical properties for further design for reliability (DfR) and precise lifetime prediction. As a fast approach to reveal the underlying mechanism, atomistic simulation studies have been reported to investigate the impact of shape, temperature, and pressure on the sintering results [9], [10]. A few studies look further into the mechanical properties of sintered structures, most focused on tension and compression simulation [11], [12]. However, in practice, nanoindentation is commonly adopted to study the mechanical properties of the sintered die-attach layer due to thin bondline thickness [13]–[15]. One main drawback of nanoindentation is that the stochastic porous microstructure leads to various results in a single specimen. Thus, it is vital to understand the nanoindentation behavior on the sintered structure from an atomistic perspective.

This paper investigated the nanoindentation behavior simulation on the sintered Cu structure. Two sintered models with different densities were created. Afterward, the impact of indentation position and indenter size on the nanoindentation response was investigated. This work bridges the pre-sinter status to the post-sinter performance by considering the testing conditions. It may pave the way to shorten the new sinter materials design, new process development, and test condition determination.

Atomistic simulation

1. Atomistic model

In this study, two Cu models with different initial packing densities were adopted for sintering and further nanoindentation study, as shown in Fig. 1. Model A is a sparse model containing 27 spherical Cu nanoparticles with a diameter of 79.112 Å. The inter-particle spacing is 7.192 Å to separate particles. A denser model was built up in model B by inserting a smaller Cu nanoparticle at the body-centered position with a diameter of 53.94 Å. The atom number of the models is 0.63M and 0.84M, respectively.

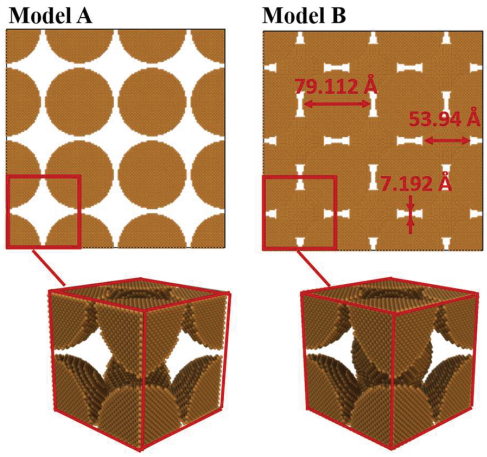

Figure 1. Atomistic models with different initial packing densities.

2. Simulation methodology

This study adopted Adam's classic embedded atom method (EAM) potential to describe the interaction between Cu atoms [16]. All simulations were conducted in a three-dimensional simulation box with periodic boundaries by Large-scale Atomic/Molecular Massively Parallel Simulator (LAMMPs) [17]. The time step was fixed as 1 fs, and the results were visualized in a 3D visualization software, OVITO [18]. The crystal atom structure was identified by common neighbor analysis (CNA) [19].

At first, the entire system was relaxed to reach its equilibrium state. The models were then sintered in the NPT ensemble at 573 K with 30 MPa applied on the simulation box for 150 ps. Subsequently, the sintered model was kept at 300 K for another 50 ps as a relaxation step. Afterward, Fig.2 shows the implementation of nanoindentation by assigning a virtual spherical indenter, initially placed 20 Å over the top surface, with a constant downward velocity of 10 m/s to the sintered model with 30 Å depth. A spherical indenter exerts a force (F) of magnitude on each atom, as shown in Equation 1

$$F(r) = -K(r-R)^2 \quad (1)$$

Where K = 10 eV/Å^3 is a specified force constant, r is the distance from the atom to the center of the indenter, and R is the radius of the indenter. The force is repulsive, and $F(r) = 0$ for $r>R$.

The thermostatic layer was assigned as 300 K in the simulation system using the NVT ensemble. Then the indentation tests were carried out with the NVE ensemble for a 50 ps indentation process and another 50 ps withdrawal process. The bottom 10 Å atoms were frozen for fixation, and the other 10 Å atoms above them were defined as thermostatic layers for temperature control. Void-centered and particle-centered positions were selected to investigate the impact of the indentation position on the indentation response, as shown in Fig. 2.

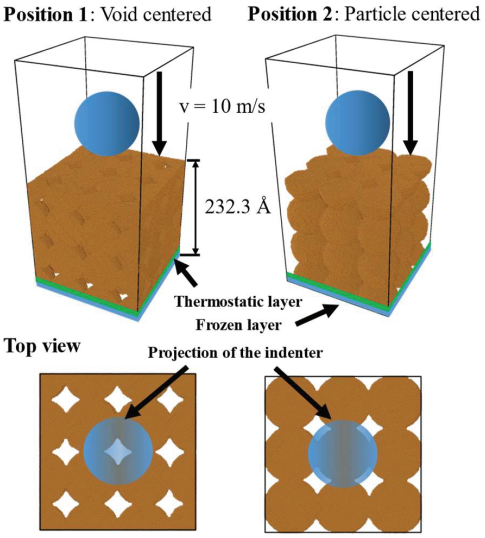

Figure 2. Schematic of nanoindentation simulation with two different positions.

Additionally, several indenter sizes were chosen to investigate the indenter size's effect on the nanoindentation behavior. As shown in Fig. 3, a scale factor η was adopted to control the projection area when the indenter was entirely indented into the sintered Cu NPs. According to the different values of η, the corresponding radius of the indenter was from 4.73 nm to 7.50 nm.

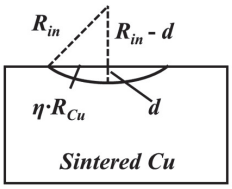

Scale factor: η
Radius of the indenter: R_{in}
Indentation depth: $d = 3\ nm$
Radius of Cu NP : $R_{Cu} = 4\ nm$

η	R_{in} (nm)
1.1	4.73
1.2	5.34
1.3	6.01
1.4	6.73
1.5	7.5

Figure 3. Definition of the different radii of the indenter

Results and discussion

1. *P-h* curves

The simulated *P-h* curves for a complete cycle of the nanoindentation process on void-centered and particle-centered positions are presented in Fig. 4. It can be seen that for the void-centered model, the load response took place later than traveling 2 nm since there was no nanoparticle beneath the indenter. The edge of the indenter would achieve the first contact with nanoparticles. In comparison, the particle-centered model responded when the displacement reached 2 nm.

The *P-h* curves present two stages. At beginning, the force increases steeply until the depth reaches about 0.8 nm, indicating a pure elastic performance. The elastic regime almost overlaps in the particle-centered position, indicating a close elastic deformation performance. Afterward, a force drop is perceived, suggesting the onset of plastic deformation. The *P-h* curves fluctuate during the loading stage, which could be attributed to the plastic rearrangement and work hardening [20]. During the withdrawal process, the load significantly drops, following a decreasing power law fitted by Oliver-Pharr, which presents a similar indentation modulus as calculated by Hertz law.

By comparing the maximum loading force, a larger indenter results in a higher loading force, and the trending is more evident in the nanoindentation in the void-centered position. In the void-centered position, the maximum load increased from 98.9 nN to 157.1 nN. In contrast, the value slight goes up from 140.4 nN to 153.1 nN in the particle-centered position. The relative porosity can be the cause for this difference. In the void-centered position, the indenter projection significantly covers more nanoparticle area on the top surface with the increase of the indenter size.

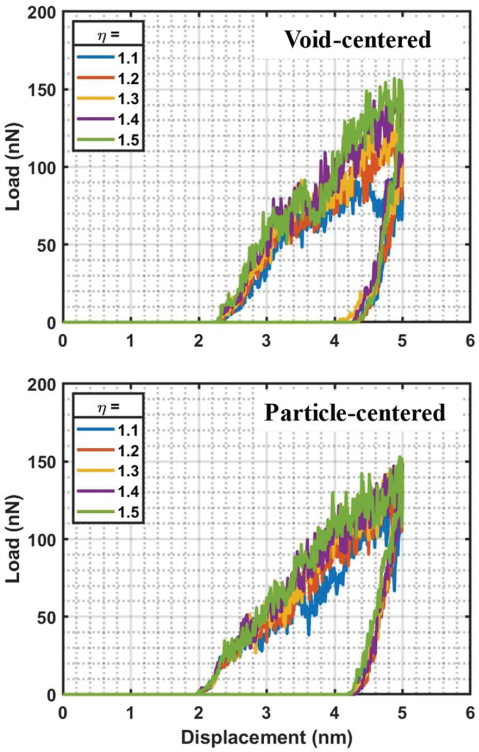

Figure 4. *P-h* curves of the sintered Model A. (top) Void-centered position; (bottom) Particle-centered position.

2. The indentation modulus of the sintered structure

The indentation modulus of the sintered structure can be fitted with the Hertz law (Eq.(2)) in the initial elastic deformation stage.

$$P = \frac{4}{3} E h^{3/2} R^{1/2} \qquad (2)$$

where P is the applied load by the indenter, R is the indenter radius, h is the indentation depth, and E is the indentation modulus.

Fig. 5 depicts the Hertz law fitting in *P-h* curves obtained from MD simulation with three different indenter sizes, indicating excellent fitting quality. The estimated indentation modulus values are summarized in Table. 1. It can be seen that the two models present different trends on the indentation modulus with a larger indenter. In the void-centered model, the maximum indentation module reaches 25.96 GPa with the largest indenter. However, in the particle-centered model, the maximum value happened with the smallest indenter. The relative porosity of the indenter projection on the top surface also causes this result. In the void-centered model, the relative porosity becomes smaller with a larger indenter; in the particle-centered model, more pores were affected with a larger indenter.

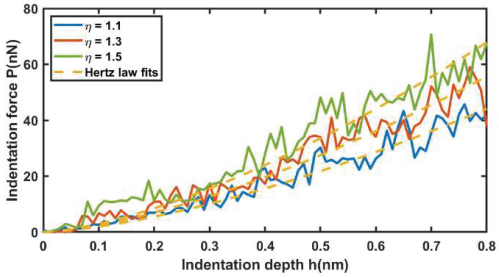

Figure 5. Hertz law fitting (orange dotted lines) in the initial elastic deformation with three different indenter sizes.

Table 1. Indentation modulus fitted by Hertz law

η	Void-centered (GPa)	Particle-centered (GPa)
1.1	21.2515	21.6111
1.2	24.3717	20.2260
1.3	23.7687	21.1169
1.4	24.4085	20.4412
1.5	25.9645	18.0340

In terms of the nanoindentation simulation on the sintered structure with different initial packing densities, porous model A and denser model B shares density of 5.61 g/cm^3 and 7.414 g/cm^3, as 59.8% $\rho_{Cu,\ bulk}$ and 82.7% $\rho_{Cu,\ bulk}$, respectively. The *P-h* curves are shown in Fig. 6 for the indention on the void-centered position. The indenter size is 7.5 nm, and η is 1.5. The blue line, red line and yellow line represent the Model A, void-centered indentation position, Model A, particle-centered indentation position and Model B, void-centered indentation position.

Fitted by the abovementioned Hertz law, Model B shows a larger indentation modulus of 55.0141 GPa with a maximum load of around 380 nN. In contrast, the maximum load is less influenced by the different indentation positions as the void-centered curve shows a similar peak to the particle-centered curve value. Compared to the more porous model A, there is no essential difference in the penetration depth when the load reaches zero in the void-centered position, indicating a similar elastic recovery in the sintered structures with different densities. In contrast, the recovered depth is more significant in the particle-centered position.

In this case, due to the porous structure, the loading response shows up after the indenter goes beneath the surface, which makes the geometry-based quantitative analysis of the elastic recovery complicated. Therefore, the analysis employed the energy perspective to study the elastic deformation in the nanoindentation process. The plastic flow was calculated as the area covered by the *P-h* hysteresis, and the elastic energy was calculated as the area covered by the *P-h* curve in the unloading process. Results show that 17.0%, 23.2 % and 15.1 % of the external work are converted to elastic energy, respectively, in different models and indentation positions. Therefore, the ratio of the external work converted elastic energy is less relevant to the global porosity than the local porosity.

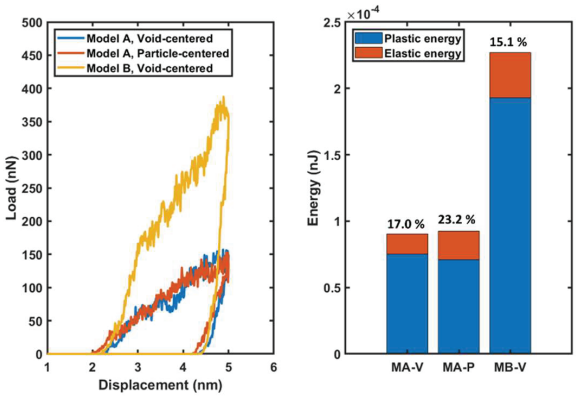

Figure 6. (Left) *P-h* curves in Model A, void-centered (MA-V) position, Model A, particle-centered (MA-P) position and Model B, void-centered (MB-V) position.; (Right) The corresponding dissipated energy

There have been no MD studies in the literature on the nanoindentation simulation on the porous sintered metallic materials. Compared to the existing reported nanoindentation experimental values, X. Liu et al. achieved an indentation modulus from 72.47 GPa to 103.02 GPa with a Berkovich indenter [21]. However, due to the size limitation in the MD simulation, the local relative porosity in the experiments is much lower than in the simulation. In contrast, X. Long et al. measured an indentation modulus of 15 GPa in sintered Ag while its bulk value is 83 GPa [13]. As an alternative test simulation, S. Wang et al. also simulated elastic modulus ranging from around 20 GPa to around 70 GPa in the compression simulation, highly depending on the porosity [22]. Thus, our simulated indentation modulus lands in a reasonable range according to other studies.

3. The hardness of the sintered structure

The hardness *H* of the sintered structure is defined as the contact pressure when a critical indentation depth has been reached, and the value stays stable with increasing loading. At a macroscopic level, the contact area can be computed according to the evolution of the diameter of the imprint. In contrast, at an atomistic level, the effective contact area is calculated based on the contact atoms with the indenter by considering the sink-in or pile-up phenomena. The atoms in contact can be calculated utilizing two spheres. Figure 7 presents the measurement of the contact area by using the following Equation 4 [23].

The hardness can be calculated from the effective contact area. Figure 8 gives the variation of hardness against the indentation depth. Like the *P-h* curves, the *H* values at first increase sharply until a certain depth of 1.25 nm and 0.5 nm in two positions, respectively (blue region). Furthermore, the *H* values become less affected by the increasing indentation depth (orange region). In the void-centered position, the simulated hardness shows slight dependence on the indenter size, while in the particle-centered position, a larger indenter reversely results in a softer value. The *H* values are summarized in Table 2.

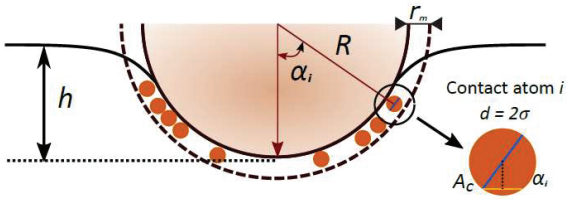

Figure 7. Illustration of calculation of effective contact area in the nanoindentation simulation. R is the radius of the indenter. rm is the lattice constant of Cu as 0.36nm, and h is the indentation depth.

$$A_c = \pi\sigma^2 \sum_{i \in contact} \cos\alpha_i \qquad (4)$$

Where σ is the atomic radius of the Cu atom at 0.128 nm, and α_i is the angle between the vector joining the center of the indenting sphere with Cu atom *i*.

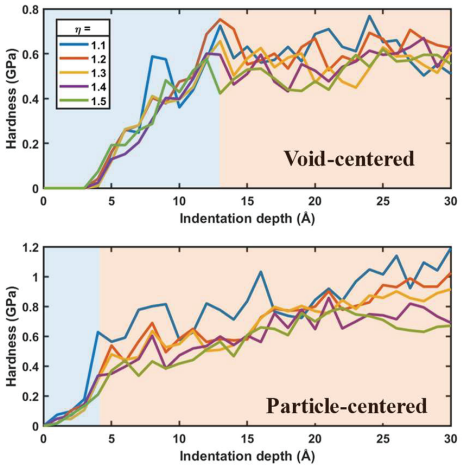

Figure 8. The hardness of the sintered Model A. (top) Void-centered position; (bottom) Particle-centered position.

Table 2. Hardness *H* of the sintered model A

η	Void-centered (GPa)	Particle-centered (GPa)
1.1	0.62	1.19
1.2	0.63	1.03
1.3	0.56	0.92
1.4	0.56	0.69
1.5	0.53	0.67

Regarding the sintered structure with different densities, Fig. 9 depicts the comparison of the projection area and hardness between model A and model B. The projection area in both models stays overlapped at the beginning until the intender touches the body-positioned nanoparticle. Despite the similar projection area, the hardness rapidly increases in model B due to a more significant loading force in the *P-h* curves in Fig. 6. As a result, the average hardness *H* in the stable stage is 0.53 GPa and 1.19 GPa for models A and B, respectively. In the experiment, J. Fan et al. [14] figured out the indentation hardness of sintered Cu NPs tends to be stable with a loading

rate larger than 0.25 mN/s and the reported experimental value is between 1.0 to 1.2 GPa, which is close to the simulated value in model B with a relatively high density.

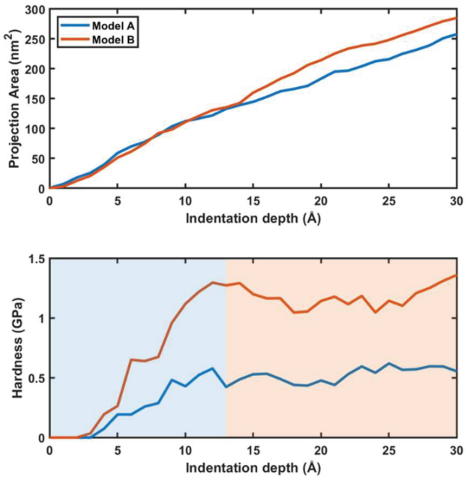

Figure 9. Projection area (top) and hardness (bottom) of model A and model B in a void-centered position with a 7.5 nm sized indenter.

4. Microstructure evolution

Figure. 10 visualizes the surface morphologies after the loading and unloading with a 7.5 nm-sized virtual indenter. The atoms are colored according to the Z position to visualize the relative distance to the top surface. At the final indentation depth, the indentation on the void-centered in both Model A and Model B presents a square affected zone caused by the plastic deformation enabled along {111}<110> slip system. It is because the central position beneath the virtual indenter is void. The indentation causes significant shear force at the contacted NP.

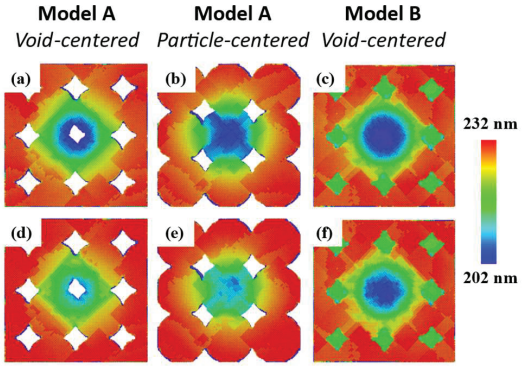

Figure 10. Z-coordinate position (a)-(c) at the final indentation depth and (d)-(f) after the unloading progress.

On the other hand, the deformation on the particle-centered position is similar to the bulk copper as a round affected area. However, the residual deformation after nanoindentation shows dependency on different model densities, as shown in Fig. 10(d)-(f). The elastic recovery of the nanoindentation in Model A is larger than Model B, and the elastic recovery of the particle-centered position is larger than the void-centered position. This result is consistent with the calculated elastic energy and plastic flow in *Section 2*.

In order to analyze the indentation mechanism in different models as well as different indentation position, the crystal structure evolution of the diagonal cross section is recorded as depicted in Fig. 11, in which the green represents face-centered cubic (FCC) atoms, red stands for hexagonal close-packed (HCP) atoms and the amorphous atoms are colored in grey. In the as-sintered atomic model in Model A, limited defects can be found in the necking region as the result of extensive atom rearrangement after the neck growth. However, a mass of stacking faults (SF) crossing the grains are figured out in the as-sintered model B. This is due to the higher sintering degree caused by a higher initial packing density, where twinning boundaries (TB) crossing the grain will be formed [24].

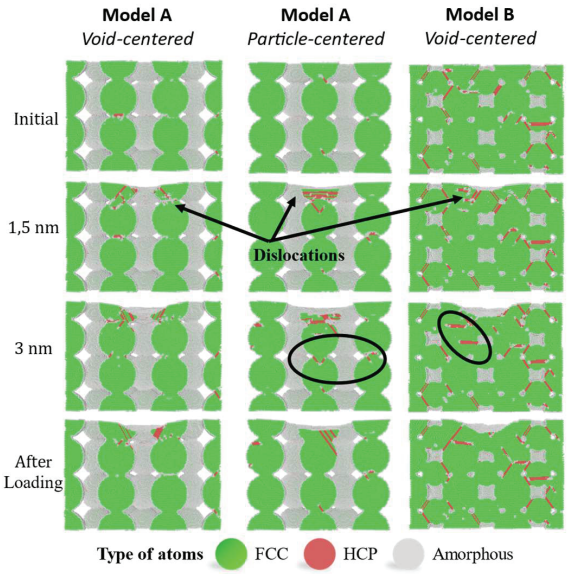

Figure 11. Microstructural evolution according to the different penetration depths of Model A with void-centered indentation position (left column); Model A with particle-centered position (middle column); Model B with void-centered position (right column)

With the indenter penetrate deeper into the sintered structure, nanoindentation on all models resemble that of a single crystalline Cu structure, which was deformed by the dislocation movement. Shockley partial dislocations are nucleated in the region beneath the indenter and around the edge of the indenter as pointed by arrows. Afterwards, the Shockley partial dislocations move forward and leave SFs behind them, which is the widely studied dislocation nucleation mechanism [25].

Meanwhile, the subsurface damage layer was increased, as denoted by the amorphous transmission from the FCC

structure, which is more evident in Model A. It is attributed to a lower energy barrier that promotes neck growth due to a lower density. After unloading progress, the microstructure undergoes an elastic recovery and atom arrangement in the affected region, leading to a slight decrease in the number of dislocations.

Also, in model A on particle-centered position and model B on void-centered position, dislocation activities on the neighbor particles' necking region were observed in the circles, meaning the sintering degree is further locally promoted. The sintering pressure is generally in the range of MPa, while the contact pressure in the indentation process can reach the range of GPa. The external work done by the indentation is likely to break the necking region's dynamic equilibrium and promote neck growth. As observed, in this nanoindentation simulation, the plastic deformation region is not only the directly contacted nanoparticles but also includes their adjacent nanoparticles.

Conclusions

This study simulated the Cu NPs sintering with different initial packing densities at 573 K with 30 MPa external pressure. The nanoindentation simulation was successfully implemented on the simulated porous structure with different nanoindentation conditions. Furthermore, the indentation modulus, projection area, and hardness were extracted from the *P-h* curves.

The indentation modulus in the void-centered position increases with the larger indenter, while in the particle-centered position, the value decreases and reaches a minimum indentation modulus of 18.03 GPa with a 7.5 nm-sized indenter. On the other hand, the hardness in the void-centered position stayed relatively stable, while the value in the particle-centered position went down when the indenter size increased. The maximum hardness was obtained with a 4.73 nm indenter in a particle-centered position as 1.19 GPa. However, the porous sintered structure with higher density resulted in better performance, as 55.01 GPa in indentation modulus and 1.19 GPa in hardness. Compared to the existing literature, the simulated indentation modulus and hardness are within the reasonable range as reported in other simulations and mechanical tests on porous sintered structures.

The elastic recovery calculated from the *P-h* curves indicated that the indentation position is more essential than the structure density, consistent with the microstructure evolution. Besides, the indentation mechanism of the plastic deformation was revealed as the dislocation nucleated in the region beneath and around the edges of the indenter. Besides, the crystal structure transformation realized an extended plastic deformation zone on the adjacent nanoparticles.

Acknowledgments

This work was supported by National Natural Science Foundation of China (52275559) and Shanghai Pujiang Program (2021PJD002).

References

[1] G. Q. Zhang, M. Graef, and F. Van Roosmalen, "The rationale and paradigm of 'More than Moore,'" *Proc. - Electron. Components Technol. Conf.*, vol. 2006, pp. 151–157, 2006, doi: 10.1109/ECTC.2006.1645639.

[2] A. I. Emon, Mustafeez-Ul-Hassan, A. B. Mirza, J. Kaplun, S. S. Vala, and F. Luo, "A Review of High-Speed GaN Power Modules: State of the Art, Challenges, and Solutions," *IEEE J. Emerg. Sel. Top. Power Electron.*, vol. 11, no. 3, pp. 2707–2729, 2023, doi: 10.1109/JESTPE.2022.3232265.

[3] H. Lee, V. Smet, and R. Tummala, "A Review of SiC Power Module Packaging Technologies: Challenges, Advances, and Emerging Issues," *IEEE J. Emerg. Sel. Top. Power Electron.*, vol. 8, no. 1, pp. 239–255, 2020, doi: 10.1109/JESTPE.2019.2951801.

[4] S. Tanimoto and H. Ohashi, "Reliability issues of SiC power MOSFETs toward high junction temperature operation," *Phys. Status Solidi Appl. Mater. Sci.*, vol. 206, no. 10, pp. 2417–2430, 2009, doi: 10.1002/pssa.200925167.

[5] B. Zhang *et al.*, "In-air sintering of copper nanoparticle paste with pressure-assistance for die attachment in high power electronics," *J. Mater. Sci. Mater. Electron.*, vol. 32, no. 4, pp. 4544–4555, 2021, doi: 10.1007/s10854-020-05196-4.

[6] H. S. Chin, K. Y. Cheong, and A. B. Ismail, "A Review on Die Attach Materials for SiC-Based High-Temperature Power Devices," *Metall. Mater. Trans. B*, vol. 41, no. 4, pp. 824–832, 2010, doi: 10.1007/s11663-010-9365-5.

[7] W. Liu *et al.*, "Recent progress in rapid sintering of nanosilver for electronics applications," *Micromachines*, vol. 9, no. 7, pp. 1–17, 2018, doi: 10.3390/mi9070346.

[8] T. F. Chen and K. S. Siow, "Comparing the mechanical and thermal-electrical properties of sintered copper (Cu) and sintered silver (Ag) joints," *J. Alloys Compd.*, vol. 866, p. 158783, 2021, doi: 10.1016/j.jallcom.2021.158783.

[9] S. Li *et al.*, "Sintering mechanism of Ag nanoparticle-nanoflake: a molecular dynamics simulation," *J. Mater. Res. Technol.*, vol. 16, pp. 640–655, 2022, doi: 10.1016/j.jmrt.2021.12.029.

[10] X. Liu *et al.*, "Coalescence kinetics and microstructure evolution of Cu nanoparticles sintering on substrates: a molecular dynamics study," *J. Mater. Res. Technol.*, vol. 17, pp. 1132–1145, 2022, doi: 10.1016/j.jmrt.2022.01.052.

[11] C. Qian, D. Hu, X. Liu, X. Fan, G. Zhang, and J. Fan, "Study on Sintering Mechanism and Mechanical Properties of Nano-Cu based on Molecular Dynamics Simulation," *2023 24th Int. Conf. Therm. Mech. Multi-Physics Simul. Exp. Microelectron. Microsystems, EuroSimE 2023*, pp. 1–9, 2023, doi: 10.1109/EuroSimE56861.2023.10100810.

[12] S. Yang, W. Kim, and M. Cho, "Molecular dynamics study on the coalescence kinetics and mechanical behavior of nanoporous structure formed by thermal sintering of Cu nanoparticles," *Int. J. Eng. Sci.*, vol. 123, pp. 1–19, 2018, doi: 10.1016/j.ijengsci.2017.11.008.

[13] X. Long, B. Hu, Y. Feng, C. Chang, and M. Li, "Correlation of microstructure and constitutive behaviour of sintered silver particles via

nanoindentation," *Int. J. Mech. Sci.*, vol. 161–162, no. July, 2019, doi: 10.1016/j.ijmecsci.2019.105020.

[14] J. Fan *et al.*, "High-temperature nanoindentation characterization of sintered nano-copper particles used in high power electronics packaging," *Results Phys.*, vol. 33, p. 105168, 2022, doi: 10.1016/j.rinp.2021.105168.

[15] X. Long, Q. Jia, Z. Shen, M. Liu, and C. Guan, "Strain rate shift for constitutive behaviour of sintered silver nanoparticles under nanoindentation," *Mech. Mater.*, vol. 158, no. September 2020, p. 103881, 2021, doi: 10.1016/j.mechmat.2021.103881.

[16] J. B. Adams, S. M. Foiles, and W. G. Wolfer, "Self-diffusion and impurity diffusion of fcc metals using the five-frequency model and the Embedded Atom Method," *J. Mater. Res.*, vol. 4, no. 1, pp. 102–112, 1989, doi: 10.1557/JMR.1989.0102.

[17] S. Plimpton, "Fast parallel algorithms for short-range molecular dynamics," *Journal of Computational Physics*, vol. 117, no. 1. pp. 1–19, 1995. doi: 10.1006/jcph.1995.1039.

[18] A. Stukowski, "Visualization and analysis of atomistic simulation data with OVITO – the Open Visualization Tool," *Model. Simul. Mater. Sci. Eng.*, vol. 18, p. 015012, 2010, doi: 10.1088/0965-0393/18/1/015012.

[19] D. Faken and H. Jonsson, "Systematic analysis of local atomic structure combined with 3D computer graphics," *Comput. Mater. Sci.*, vol. 2, pp. 279–286, 1994.

[20] J. Li, B. Lu, Y. Zhang, H. Zhou, G. Hu, and R. Xia, "Nanoindentation response of nanocrystalline copper via molecular dynamics: Grain-size effect," *Mater. Chem. Phys.*, vol. 241, no. August 2019, p. 122391, 2020, doi: 10.1016/j.matchemphys.2019.122391.

[21] X. Liu, "Pressure-assisted Cu sintering for SiC die-attachment application," 2023.

[22] S. Yang, W. Kim, and M. Cho, "Molecular dynamics study on the coalescence kinetics and mechanical behavior of nanoporous structure formed by thermal sintering of Cu nanoparticles," *Int. J. Eng. Sci.*, vol. 123, pp. 1–19, 2018, doi: 10.1016/j.ijengsci.2017.11.008.

[23] S. P. Patil, V. G. Parale, H. H. Park, and B. Markert, "Molecular dynamics and experimental studies of nanoindentation on nanoporous silica aerogels," *Mater. Sci. Eng. A*, vol. 742, no. October 2018, pp. 344–352, 2019, doi: 10.1016/j.msea.2018.11.019.

[24] D. Hu, Z. Cui, J. Fan, X. Fan, and G. Zhang, "Thermal kinetic and mechanical behaviors of pressure-assisted Cu nanoparticles sintering: A molecular dynamics study," *Results Phys.*, vol. 19, no. October, p. 103486, 2020, doi: 10.1016/j.rinp.2020.103486.

[25] J. Li *et al.*, "Study of nanoindentation mechanical response of nanocrystalline structures using molecular dynamics simulations," *Appl. Surf. Sci.*, vol. 364, pp. 190–200, 2016, doi: 10.1016/j.apsusc.2015.12.145.